BioMACROMOLECULES

Subscriber access provided by UNIV DE VALLADOLID

Article

A Self-Organized ECM-Mimetic Model Based on an Amphiphilic Multiblock Silk-Elastin-Like co-Recombinamer with a Concomitant Dual Physical Gelation Process

Alicia Fernández-Colino, F. Javier Arias, Matilde Alonso, and José Carlos Rodriguez-Cabello

Biomacromolecules, **Just Accepted Manuscript** • Publication Date (Web): 17 Sep 2014

A Self-Organized ECM-Mimetic Model Based on an Amphiphilic Multiblock Silk-Elastin-Like co-Recombinamer with a Concomitant Dual Physical Gelation Process

*Alicia Fernández-Colino, F. Javier Arias, Matilde Alonso, J. Carlos Rodríguez-Cabello**

G.I.R. Bioforge, University of Valladolid, CIBER-BBN, Paseo de Belén 11, 47011 Valladolid, Spain

ABSTRACT. Although significant progress has been made in the area of injectable hydrogels for biomedical applications and model cell niches, further improvements are still needed, especially in terms of mechanical performance, stability and biomimicry of the native fibrillar architecture found in the extracellular matrix (ECM). This work focuses on the design and production of a silk-elastin-based injectable multiblock co-recombinamer that spontaneously forms a stable physical nanofibrillar hydrogel under physiological conditions. That differs from previously reported silk-elastin-like polymers on a major content and predominance of the elastin-like part, as well as a more complex structure and behavior of such part of the molecule, which is aimed to obtain well defined hydrogels. Rheological and DSC experiments showed that this system displays a coordinated and concomitant dual gelation mechanism. In a first stage, a rapid, thermally driven gelation of the co-recombinamer solution takes place once the system reaches body temperature due to the thermal responsiveness of the elastin-like (EL) parts and the amphiphilic multiblock design of the co-recombinamer. A bridged micellar

structure is the dominant microscopic feature of this stage, as demonstrated by AFM and TEM. Completion of the initial stage triggers the second, which comprises a stabilization, reinforcement, and microstructuring of the gel. FTIR analysis shows that these events involve the formation of β-sheets around the silk motifs. The emergence of such β-sheet structures leads to the spontaneous self-organization of the gel into the final fibrous structure. Despite the absence of biological cues, here we set the basis of the minimal structure that is able to display such a set of physical properties and undergo microscopic transformation from a solution to a fibrous hydrogel. The results point to the potential of this system as a basis for the development of injectable fibrillar biomaterial platforms towards a fully functional, biomimetic, artificial extracellular matrix and cell niches.

KEYWORDS. Elastin-like recombinamers, SELR, hydrogel, fibrillar, artificial extracellular matrix .

INTRODUCTION

The latest trends in materials science involve the strategy of copying the designs found in Nature in the laboratory [1], since they exhibit extraordinary properties that have been achieved over millions of years of evolution. Within this framework, the greatest biomaterials-related challenge in the field of tissue engineering is to create biomimetic scaffolds that can act in a similar manner to the extracellular matrix (ECM). Given the complexity of the natural ECM, this is a particularly challenging task as the artificial ECM (aECM) must reproduce the complex cell-ECM interaction, which includes specific cell adhesion, protease sensitivity, and cytokine release, amongst others. In addition, cell-material interactions and the group of factors that govern cell fate in the natural ECM are not restricted exclusively to biological features, since physical clues are also of relevance. From a structural perspective, the ECM has a fibrillar and viscoelastic character, and such biophysical features have been reported to have a significant influence on cell behavior [2-4]. Although the molecular pathways involved in cellular

mechanosensitivity are still open to investigation, it is well known that cells sense and respond to the stiffness of their environment by converting mechanical inputs into chemical outputs [5,6]. More recently, cell fate related to energy dissipation mediated by enzymatic ECM degradation has also been reported [7]. Such discoveries highlight the importance of controlling both the more obvious biological environment of a bioengineered matrix and the physical one.

One more condition must be added to all those mentioned above, namely that candidate aECMs will eventually be implanted, therefore, in addition to being sufficiently functional, they must satisfactorily cope with the immune rejection system and not be identified as a foreign body. Furthermore, they should be reabsorbed without any damage or stress for growing cells. In light of the above, the creation of such aECMs seems to be a major challenge, and more so if we consider that all this must be achieved in an injectable formula, in other words a system in a liquid state from which, after implantation (injection), all other structures and functions develop; self-organization is a must in this context.

One interesting group of self-assembling polymers is the elastin-like polymers, and particularly their recombinant versions, the elastin-like recombinamers (ELRs) [8]. ELRs are protein-based materials whose composition is inspired by the primary sequence found in natural elastin. Thus, the amino-acid sequence of ELRs is commonly constituted by repeats of the (VPGXG) pentapetide, where X is any amino acid except proline. ELRs show a reversible LCST (Lower Critical Solution Temperature) phase transition, usually known as the inverse temperature transition (ITT) in the context of elastin-like materials, in response to temperature. In an aqueous medium, below a characteristic temperature known as the transition temperature (Tt), the polymer chain remains soluble. However, above this Tt, the ELR assembles hydrophobically and adopts a regular, dynamic, nonrandom structure characterized by the presence of type II β turns [9,10]. Such stimuli-responsive behavior, together with their proven biocompatibility [11] and their mechanical performance, have positioned these recombinant

macromolecules as potential candidates for use in numerous biomedical applications [12,13], particularly regarding the development of injectable hydrogels, which mainly relies on their ability to respond to thermal stimulation. As a result of this property, the recombinamer solution can be injected as a liquid but, once inside the organism, it reaches body temperature and consequently undergoes a phase transition from solution to gel that can be referred to as thermo-gelling. In general, homo-ELRs tend to segregate from solution, thus giving rise to a coacervate. However, for a more effective hydrogel formation, ELRs have been designed as multi-block amphiphilic molecules [14]. Thus, the hydrophilic blocks, which do not show LCST behavior under the conditions used, are responsible for water retention, whereas the cross-linking function is achieved by the thermally driven folding and hydrophobic interaction of the hydrophobic blocks. Following this idea, a thermally controlled amphiphilic ELR tetrablock co-recombinamer in which the hydrophobic blocks, which contain isoleucine as guest residue, are responsible for the physical cross-linking by means of a bridged micelle structure at a microscopic level, has been reported previously [14]. Glutamic acid is the guest residue in the remaining two hydrophilic blocks. However, these hydrogels does not show a fibrillar structure upon setting. Additionally, they lose their integrity in contact with an excess of aqueous medium. Under those conditions, the gel swells and, finally, at a molecular level, the material goes from a crosslinked hydrogel to a micellar dispersion. The weak character of noncovalent interactions is the problem common to most physical crosslinking approaches [15-18].

With regard to the fibrillar architecture, polymer processing technologies such as electrospinning have been applied to obtain fibers on the nanometric scale [19]. However, the main handicap of this approach is to place cells within a nanofibrillar structure with pore sizes smaller than cellular diameters. As a result, strategies that allow nanofibrillar networks to be formed *in situ* are preferred. An excellent approach for obtaining nanofibers takes advantage of molecular self-assembly [20 21]. In this regard, researchers have fixed their attention on self-assembled motifs present in Nature, such as coiled-coiled structures, β-sheet

structures, or β-hairpins and have incorporated such designs, sometimes with suitable modifications, to obtain nanostructures with a well-defined shape.

In this context, SL motifs have been reported to spontaneously adopt a β-sheet structure, which is characterized by its stability [22,23]. The stable nature of the β-sheet conformation adopted, together with their biocompatible nature, has propelled the development of a wide range of silk-inspired materials [24,25] and silk-elastin inspired materials. SELRs have already proven to display a synergic effect in which the elastin-like (EL) part, which tends to have a relatively simple composition in the examples found in the literature, reduces the degree of crystallinity of the SL blocks while enhancing the elastic properties of the combination [26]. However, the stimuli-responsiveness of the EL block has not been exploited to any great extent to date and no complex molecular designs for that block showing advanced functionality have been reported. Furthermore, many SELR designs incorporate such a high SL percentage that the contribution of the elastomeric portion to the self-assembly process is imperceptible [27,28]. However, experience with SELR designs with a lower SL content has demonstrated that, in such compositions, the EL blocks are able to maintain their characteristic thermal transition [28-30]. One of the main drawbacks associated with the use of SL motifs as physical crosslinking domains to obtain injectable hydrogels is that the kinetics of β-sheet formation under physiological conditions (aqueous medium, neutral pH and 37°C) is too slow [31]. This is clearly different from the kinetics of ELR self-assembly, which is practically instantaneous above Tt. An interesting example of SELRs explored for their capacity to show dual elastin and silk associations have been reported [28]. Nevertheless, in that work the ratio SL to EL ranged between 15% to 60% so the portion of SL blocks was high and clearly dominated the self-assembling properties of the molecule giving no much space for exploiting the self-assembling peculiarities of the EL blocks.

The main aim of this work is to test the possibility of combining the two kinds of self-assembly processes to achieve an advanced system in which structure development appears in a multistage and predefined sequence with a major contribution to the self-assembling process of the EL part of the molecule, which in addition will show a more complex amphiphilic molecular architecture and a higher propensity to form stable hydrogels than the previously reported SELRs. Under this general idea we seek to obtain a material that, first, an increase in temperature triggers the assembly of EL- blocks (rapid hydrophobic association), second, the association of the EL blocks triggers the subsequent association of the silk blocks (β-sheet formation) and, simultaneously, fibrillar structures emerge upon maturation of the β-sheet associations.

A new SELR has been designed, produced, and studied to test this hypothesis. The composition of this SELR is dictated by a reductionist approach in which the minimal structure displaying the desired physical properties is the subject of study, thereby avoiding the incorporation of bioactive domains, that can be added later to fully develop the final functionality of the system. The dynamics of gelation, the interdependence among stages, the mechanical properties of the thus-formed hydrogels, and the structural characteristics at a microscopic and molecular level are reported in this work.

MATERIALS AND METHODS.

Construction of (EIS)x2 (SELR) and (EI)x2 (ELR)

Gene synthesis was carried out using standard molecular biology protocols. DNA sequences encoding each monomer were contained in a modified version of the cloning vector pDrive (Qiagen), named as pDAll, characterized by the engineering of two inverted Eam 1104 I and one SapI restriction sites in the poly-linker region. Thus, the DNA sequence encoding each monomer cloned in pDAll vector is flanked

by Eam 1104 I and SapI recognition sites in 5´ termini and Eam 1104 I site at 3´ termini. Sequential introduction of the repetitive EL or SL polypeptide-coding gene segments to form fusion genes with a fully controlled composition and chain length was carried out using a "recursive directional ligation" (RDL) strategy, by using the rectriction type II enzymes Eam 1104 I and SapI . The sequences were verified by agarose gel electrophoresis of the restriction fragments generated after enzymatic digestion and automated DNA sequencing. Selected genes were sub-cloned into a modified version of pET-25(+) expression vector.

(EIS)x2 production and purification

The modified version of pET-25(+) expression vector containing our gene construction was transformed into the *E.coli* strain BLR(DE3)star (Invitrogen). The resulting recombinant strain was grown at 37ºC in the auto-induction medium (Terrific broth) in a 15L bioreactor (Applikon), reaching optical density values up to 8 at 600 nm after 12 h. Immediately after, cells where recovered by centrifugation at 4ºC, and the cell pellets were resuspended in saline buffer prior disruption (Constant Cell Disruption System). The resulting soluble fraction obtained after centrifugation was subjected to the purification steps, The purification protocol consisted of sequential rounds of inverse transition cycling (ITC) optimized according to the specific characteristics of the (EIS)x2 co-recombinamer. The purity and molecular weight of the co-recombinamer were routinely determined by sodium dodecyl sulfate polyacrylamide gel electrophoresis (SDS-PAGE) and mass spectrometry (MALDI-TOF/MS). The amino acid composition was further verified by HPLC analysis. NMR analysis was also carried out in order to ensure the absence of non-proteinaceous organic impurities.

Visualization of the sol-gel behavior

In order to check the ability of both recombinamers to rapidly form hydrogels upon increasing the temperature, 15 wt. % aqueous solutions of (EIS)x2 and (EI)x2 were prepared by dissolving the pure recombinamers in PBS at 4ºC for 6 h. Once the recombinamers were in a sol state at 4ºC, they were placed at room temperature. After one minute, the samples were inverted and pictures were taken.

A solution of (EIS)x2 co-recombinamer at 15 wt. % was loaded into a syringe at 4°C and the tip of the syringe removed with a knife. The syringe plunger was then depressed to deposit the co-recombinamer solution into the aqueous PBS medium at 37°C. In parallel, a solution of (EI)x2 co-recombinamer was subjected to the same procedure as negative control. Photographs were taken at different times in order to monitor the evolution of the formed hydrogels.

In order to check the injectability, a 15 wt.% solution of the (EIS)x2 co-recombinamer at 4°C was loaded into a syringe and injected into an aqueous PBS solution at 37°C and neutral pH. Needles with diameters ranging from 18G to 23G were used.

Macroscopic properties: Thermal properties

We decided to use the DSC technique to monitor the formation of irreversible physical cross-links in the (EIS)x2 co-recombinamer. DSC experiments were performed using a Mettler Toledo 822e with liquid-nitrogen cooler. Both temperature and enthalpy were calibrated with a standard sample of indium. The solutions for the DSC experiments were prepared at 5, 10 and 15 wt.% in an aqueous buffered solution (PBS). 20 μL of the corresponding solution was placed inside a standard 40-μL aluminum pan, sealed hermetically, and subjected to annealing treatments comprising incubation at fixed temperatures (5, 10, 15, 25, 37, 60°C). The samples were analyzed by DSC at different times. The heating program for DSC

experiments included an initial isothermal stage (5 min at 0°C for stabilization of the temperature and the state of the recombinamers), followed by heating at 5°C/min from 0°C to the desired temperature range. The same rate was applied for cooling processes. The enthalpy values for endothermic processes were taken as negative and exothermic values as positive.

In order to quantify the progression rate of the irreversible folding mediated by SL blocks, the normalized ratio between the secondary peak (I_2) and the main peak (I_1) was plotted versus time. These curves were fitted to a first-order kinetics, and the rate constant "k" for each annealing temperature was obtained. The temperature-dependence of "k" was analyzed using an Arrhenius equation.

$$k = A \cdot e^{-\frac{Ea}{R \cdot T}}$$

In the above, "k" is the kinetic constant, "A" is the pre-exponential factor, "R" is the Universal gas constant (8.3 J/mol·K), "Ea" is the activation energy (expressed in J/mol), and "T" is the temperature (in kelvin).

Macroscopic properties: Rheology

The mechanical properties of the hydrogels were determined using rheological tests in a controlled stress rheometer (AR2000ex, TA Instruments) equipped with a Peltier plate temperature control.

Conversion of the solution to a gel, known as the sol-gel process, was studied for both (EI)x2 and (EIS)x2. A parallel plate geometry with a diameter of 20 mm and a sample volume of 350μL in PBS was used. The temperature ramp and gelation kinetics were carried out at a constant strain of 0.1% and a frequency of 1 Hz. Temperature ramp experiments were performed in the concentration range 5-15

wt.% by heating the sample from 5 to 37°C at a rate of 2.5°C/min; the reverse process (cooling) was performed under the same conditions. The gelation kinetics were measured at 37°C.

The active involvement of the SL blocks in the mechanical performance of the hydrogels was studied. To this end, (EIS)x2 was dissolved at 5, 10 and 15 wt.% at 4°C for 6h, and the resulting solutions placed in a mold, sealed, and incubated at 37°C for a period of 1, 2, 5, and 10 days. After this time the hydrogels (referred to as hydrogels with annealing) were measured in the rheometer at 37°C and 5°C using a parallel plate geometry (20 mm diameter). Measurements of G' (elastic or storage modulus) and G" (viscous or loss modulus) were performed by varying the frequency (between 0.1 and 10 Hz) in a constant strain mode (0.1%). Bulk elastic modulus "K" was calculated by applying the relation between "G", "K", and the Poisson coefficient (υ) [32]. Poisson coefficient was estimated to be 0.49 [33] (Supplementary Information).

Molecular level: FTIR analysis

Possible conformational changes in (EIS)x2 due to the annealing treatment were evaluated by FTIR. To this end, an (EIS)x2 hydrogel annealed for 3 days and 5 days at 37°C was dried in an oven at 37°C in order to obtain a film and thus avoid the interference of water with the FTIR measurement. Moreover, since methanol treatment promotes folding in β-sheets, an additional sample, the preparation of which involved annealing for 5 days, similar to the previous sample, and an additional treatment with 70% methanol for two hours, was measured. Freeze-dried pure co-recombinamer without any annealing treatment was also checked as negative control and compared with the (EI)x2 co-recombinamer.

Fourier Transform Infrared spectroscopy (FTIR) analysis was performed using a Bruker Tensor 27 spectrometer. For each measurement, 512 scans were co-added with a resolution of 2 cm^{-1} in the

wavenumber range from 1400 to 1800 cm^{-1}. The statistical significance of the peak shifts observed was estimated by a two-way ANOVA followed by Tukey's multiple comparisons test.

Dynamic Light scattering (DLS)

Dynamic light scattering measurements were performed using a BI-200SM multiangle goniometer (Brookhaven Instrument, Holtsville, NY) with a 33mW He−Ne vertically polarized laser at a wavelength of 632.8 nm and a digital correlator (BI-9000AT).

Solutions of (EI)x2 and (EIS)x2 were prepared by dissolving pure, lyophilized products in MilliQ water with 0.05% sodium azide to a concentration of 25 μM. These solutions were kept at 4 °C overnight to allow complete dissolution of the proteins. The samples were incubated at 37ºC to allow supramolecular assembly to occur, and measured at different time intervals. DLS measurements were performed at a scattering angle of 90°C. Co-recombinamer solutions at a concentration of 25 μM were introduced into glass cells and stabilized for 10 min at the fixed temperature (5 or 37°C) in a thermostatted decalin bath.

Volume distributions were determined using a Zetasizer nano ZSP (Malvern Instruments) equipped with a 10 mW He−Ne laser at a wavelength of 633 nm. Samples were introduced into polystyrene cuvettes and stabilized for 10 min at the desired temperature. Size was obtained from the correlation function, by using Cumulant analysis.

Transmission electron microscopy (TEM)

Nanostructure formation was checked by TEM. Solutions of (EI)x2 and (EIS)x2 were prepared by dissolving pure, lyophilized products in MilliQ water to a concentration of 25 μM. These solutions were

kept at 4 °C overnight to allow complete dissolution of the proteins. To prevent biological contamination, azide was added to a final concentration of 0.05% The sample was incubated at 37ºC to allow supramolecular assembly to occur, and an aliquot was taken and measured at different time intervals (0, 48 and 96 hours and 7 months). TEM measurements were performed using a JEOL JEM-1230 electron microscope operating at 120 kV. The specimens were prepared by placing a drop of the solution on a plasma-treated carbon-coated copper grid, followed by water evaporation at 37ºC.

Atomic Force Microscopy (AFM)

Stock solutions of (EI)x2 and (EIS)x2 were prepared by dissolving pure, lyophilized products in PBS to a concentration of 25 μM. These solutions were kept at 4°C overnight to allow complete dissolution of the proteins. To prevent biological contamination, azide was added to a final concentration of 0.05%. A drop (50 μL) of each co-recombinamer at each tested condition (without annealing and with 7 months of annealing at 37ºC) was deposited onto a clean graphite (HOPG) surface and dried at 37°C. The dried samples were analyzed using a Multimode 8 AFM attached to a Nanoscope V electronics (Bruker) in tapping mode.

RESULTS AND DISCUSSION.

Construction of (EIS)x2 (SELR) and (EI)x2 (ELR)

The amino-acid sequences of the different constructs (EI)x2 and (EIS)x2 used here are, respectively, (1) MESLLP-{[(VPGVG)2-(VPGEG)-(VPGVG)2]10[VGIPG]60}2-V and (2) MESLLP-{[(VPGVG)2-(VPGEG)-(VPGVG)2]10[VGIPG]60)-[V(GAGAGS)5G]2}2-V. (EI)x2 is the control ELR, which has

the same EL composition as (EIS)x2 but lacks the SL blocks. The construction and purification of (EI)x2 has already been reported [14]. With regard to (EIS)x2, sequential introduction of the repetitive polypeptide-coding gene segments to form fusion genes with a fully controlled composition and chain length was carried out using the recursive directional ligation (RDL) technique [34,35]. DNA sequencing and restriction mapping analysis showed the correctness of the gene-construction process (Data not shown).

(EIS)x2 production and purification

(EIS)x2 was successfully purified using by an optimized inverse temperature cycling (ITC) [36] protocol. Production yields of around 170 mg per liter of bacterial culture were achieved. The final product was characterized by SDS-PAGE electrophoresis (Figure S1), MALDI-TOF mass spectrometry (Figure S2), amino acid analysis (Table S1), and NMR spectroscopy (Figure S3), which confirmed the purity and correctness of the biosynthetic process in terms of sequence and molecular mass (See Supporting Information).

According to the literature, many SELRs have been purified by different methods that invariably comprise a chromatographic step [37]. However, chromatography is expensive, requires specialized equipment and is difficult to scale up, therefore alternative protocols are preferred. As such, simplified purification protocols based on the use of acidic pH combined with ammonium sulfate precipitation have been developed [38]. Although the stimuli-responsive behavior of ELRs is maintained upon incorporation into a chimeric fusion protein [39,40], such behavior has not been exploited as a feasible option for SELR purification since temperature accelerates the irreversible gelation process mediated by SL folding. Nevertheless, we have successfully made use of the reversible inverse transition of the elastomeric part of (EIS)x2 from soluble to insoluble and, as a result, have managed to purify (EIS)x2

using inverse transition cycles. This finding is likely motivated by the proportion of SL blocks to EL blocks used in this construct, which is relatively small (the EL blocks clearly dominate the final structure) compared to other SELRs found in the literature. This method entails a number of advantages, such as low cost and scalability. To the best of our knowledge, this is the first time that a SELR has been purified using such an approach.

Visualization of the sol-gel behavior

15% aqueous solutions of both co-recombinamers have demonstrated their ability to rapidly form hydrogels with increasing temperature (Figure 1, a - d). In principle, both co-recombinamers behave the same and display a sol-gel transition as the temperature is increased.

In most physical hydrogels, an excess of water acts as a destabilizing agent for the network of noncovalent interactions, therefore their exposure to fluids is considered to have adverse effects. In our case, upon exposing the two gels to such a detrimental environment, and despite the initial similarities, the two gels display clear differences. To check the stability of (EI)x2 and (EIS)x2 in the presence of an excess of aqueous medium, 15 wt.% solutions of both recombinamers at 4ºC were directly added to an aqueous PBS medium (pH 7) at 37ºC, as described in the Experimental Section. As shown in Figure 1 e, after adding the cold solution to the warm aqueous medium, both solutions promptly showed the formation of a hydrogel. However, the stability of these hydrogels with time was clearly different, exhibiting striking differences after incubation for only 1 day under these conditions. Thus, the (EI)x2 hydrogel disaggregated completely and no signs of it were evident, with only a slightly turbid solution remaining (Figure 1 f). In contrast, the (EIS)x2 hydrogel did not disaggregate but acquired a more robust appearance (Figure 1 g). This latter hydrogel remained stable for at least two months under those conditions (Figure 1 , j) and, from the very beginning and up to the end of the experiment, displayed

sufficient consistency to be easily manipulated (Figure 1 k). Hydrogel degradation was estimated to be 10% (Suplementary information. Figure S 6).

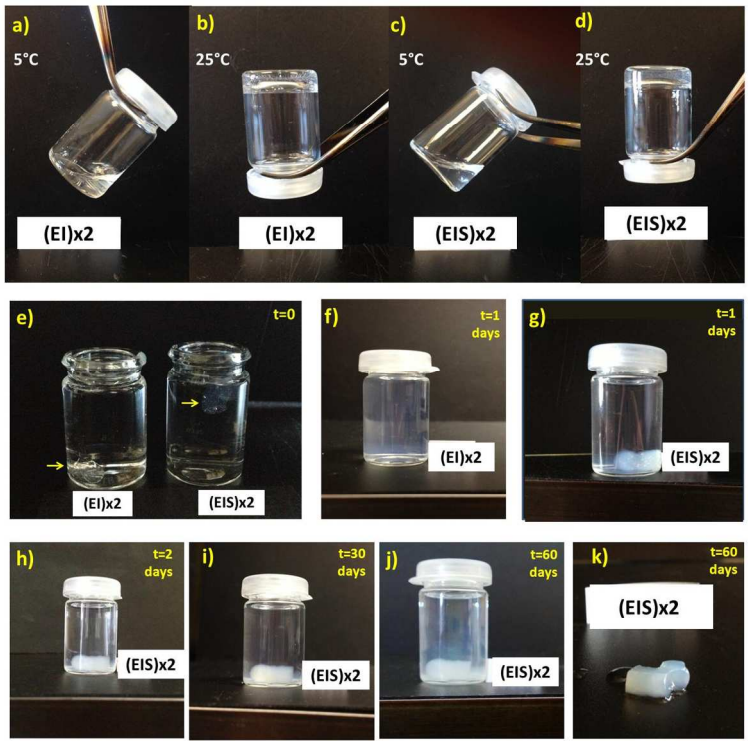

Figure 1: Pictures showing both the ability to rapidly form hydrogels upon increasing the temperature and the stability features of (EI)x2 and (EIS)x2: a) aqueous solution of EI)x2; b) (EIS)x2 hydrogel formed upon increasing the temperature; c) aqueous solution of (EIS)x2; d) (EIS)x2 hydrogel formed upon increasing the temperature; e) picture taken just after addition of the co-recombinamer solutions to the aqueous medium in a 3 mL glass vial; f) to j) pictures taken at different times after adding the co-recombinamer solutions to the aqueous medium (PBS) in a 3 mL glass vial. k) (EIS)x2 hydrogel removed from the aqueous medium after two months.

The existence of a gelation triggered by a temperature increase suggests the possibility of using these hydrogels, and especially (EIS)x2 due to its increased stability, as injectable systems in minimally invasive therapeutic approaches. As such, the injectability of a 15 wt.% (EIS)x2 solution (in PBS at 10ºC) was checked using a battery of needles of different diameters. G18, G19, G21, and G23 needles

were tested and it was found that the samples were very easily injected using needles of diameters G18 and G19 and they could also be injected without difficulty using a G21 needle. In contrast, injection using a G23 needle was unsuccessful.

Consequently, all the general properties qualitatively shown above point to the potential of (EIS)x2 as a very attractive candidate for use in biomedical applications, where injectability and rapid *in situ* gelation are required, without any restrictions with regard to exposure to fluids.

In order to quantify the behavior observed upon the visual inspection of both gels, their thermal and mechanical properties at the macroscopic level were first studied.

Macroscopic properties: Thermal properties

The thermal properties of the hydrogels produced by these materials were studied by DSC. DSC has proven to be an adequate technique to quantify the ITT, providing values for both the Tt and latent heat (ΔH). DSC scans were carried out on both (EIS)x2 and (EI)x2 solutions, as detailed in Materials and Methods. Figure 2 shows the thermograms for (EIS)x2 (a and b) and (EI)x2, which was used as control (c and d). The thermograms labeled with as "0 h" correspond to the thermal behavior found for the freshly dissolved co-recombinamers. The Tts estimated from the peak temperatures were 14.4°C for (EIS)x2 and 13.0 °C for (EI)x2, and the associated enthalpies for such ITTs were 8.2 and 9.1 J/g, respectively. The presence of the hydrophilic amino acid serine in the sequence of the SL motif could be responsible for the observed increase in Tt and subsequent decrease in enthalpy of (EIS)x2 with respect to (EI)x2. According to the literature, the ITT of the hydrophobic block (VGIPG) in (EI)x2 leads to a gel state [14]. Such gelation is fully reversible since the sol state is recovered simply by lowering the temperature below its Tt. The similarity in terms of Tt and enthalpy values, and the similarity of their

shapes, leads us to conclude that, for the freshly dissolved solutions, (EIS)x2 presumably experiences a thermogelling process similar to that displayed by the control (EI)x2, with the effect of the SL block being restricted to a modest shift in the Tt and ΔH values. Moreover, the reversibility of the measured thermodynamic process provides further evidence for the correspondence of such process with the ITT of the (VGIPG) blocks present in (EIS)x2 (Figure 2, a and b).

However, when used as an implantable system, this hydrogel will be subjected to a relatively prolonged isothermal state at 37ºC during its service time. Therefore, to determine whether the system can experience a change in properties during that period, a set of samples annealed at 37ºC for different times were also studied by DSC. The changes in the shape of the thermogram for (EIS)x2 are evident and dependent on the annealing time. Thus, after incubation at 37°C for 15 h, the endothermic peak becomes broader and is characterized by the incipient appearance of a shoulder or secondary endotherm at lower temperatures. At longer annealing times the shape of the endotherm evolves further and the presence of the secondary peak at a temperature of 11.0°C becomes increasingly clear. After annealing at this temperature for 63 h the new peak at 11.0°C becomes the main one, leaving only a slight trace of the peak previously seen at 14.4°C. From 87 h on, the shape of the thermogram appears to remain unchanged. These results contrast with the behavior of (EI)x2, which exhibited neither peak broadening nor the appearance of a secondary peak at any annealing time (Figure 2, c and d).

On the other hand, the endothermic peak and its associated ITT measured for each annealing time were totally reversible and, in a heating-cooling cycle, the endothermic peak transformed into an exothermic peak with an identical ΔH and only minor differences in Tt that can easily be explained on the basis of the thermal lag of the experimental setup. Moreover, on cooling, this exothermic peak displayed the same shape as its counterpart endothermic peak for each fixed condition (co-recombinamer and annealing time). Such reversibility further reinforces the association of these endotherms in heating and their corresponding cooling exotherms with the EL-block ITT. In addition, since the only difference

between (EI)x2 and (EIS)x2 is the presence of SL blocks in the latter, it can be concluded that the variation in the shape of the thermogram, which occurs with increasing annealing time at 37°C, must be caused by the presence of this block, which somehow exerts an influence on the ITT.

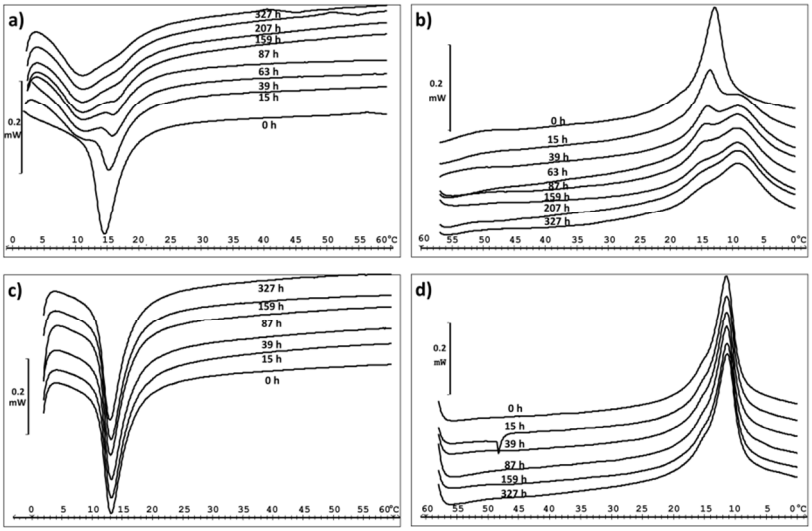

Figure 2: DSC scans for 15 wt.% (EIS)x2 and (EI)x2 solutions after annealing at 37˚C for different times. (a) DSC thermograms for heating and (b) cooling processes for (EIS)x2 after annealing at 37 ºC for. 0, 15, 39, 63, 87, 159, 207 and 327 h. Note the variation in the thermogram shape along annealing time. (c) DSC thermogram for heating and (d) cooling processes for (EI)x2 co-recombinamer solution after annealing at 37 ºC for 0, 15, 63, 87, 159, and 327 h. For (EI)x2, thermogram shape remained unchanged.

It can be concluded that annealing at 37ºC causes the (EIS)x2 gel to split into a bimodal state. Annealing causes the emergence of a new state in (EIS)x2 that is characterized by a lower Tt. At a molecular level, this must mean that EL blocks in such a state exhibit a lower effective mean polarity, as can be deduced

by the shift in Tt to lower values [41]. Although both states seem to coexist, the increase in annealing time seems to promote growth of the state with lower Tt at the expense of the initial one.

Macroscopic properties: Rheology

Macroscopic observation of the systems clearly indicated that freshly prepared solutions of both co-recombinamers undergo a rapid gelation process upon increasing their temperature above their Tt.

Early gelation due to the thermally triggered transition of the (VGIPG) blocks.

In order to quantify the resulting mechanical properties, freshly prepared 15 wt.% (EI)x2 and (EIS)x2 (no annealing) solutions were subjected to a rheological study consisting of heating from 5 to 37°C at a rate of 2.5°C/min.

Many criteria have been used in the literature to estimate the gel point [14,42,43]. The crossover between G´ and G´´ is usually considered to indicate the gelation point [43]. However, the crossing point depends on the frequency of the oscillatory experiment and, as a consequence, might be close, but not identical, to the Tt [44]. As such, the gel point was estimated here as the temperature where tanδ shows a peak since such a peak is a direct consequence of the molecular rearrangement of the co-recombinamers due to their characteristic ITT.

As shown in Figure 3 (a and c), gel formation unequivocally occurred for both samples in the temperature range from 10°C to 20°C, which is evident for both the G´,G´´ and tanδ plots. The maximum storage moduli displayed were $1.1 \cdot 10^3$ Pa and $2.5 \cdot 10^3$ Pa for (EI)x2 and (EIS)x2, respectively. When a cooling ramp from 37°C to 5°C was applied to the same samples, the shear modulus decreased, reaching values close to 0 Pa at 5°C (Figure 3 b and d). This reversibility of the

gelation process is in agreement with the fact that the increase in modulus was a consequence of the reversible transition of the EL block (VGIPG). The observed increase in the storage modulus indicates that, although they were not responsible for this reversible gelation, SL motifs did have an effect on the final characteristics of the hydrogel formed as a result of the reversible transition of the elastomeric portion.

The values of the loss factor (tanδ) showed a maximum at 13.0°C and 15.8°C for (EI)x2 and (EIS)x2, respectively, and such values would be considered to be representative of the transition from liquid to gel determined by rheological methods [45], since EL moieties undergo conformational changes from an extended state to a folded one as the ITT takes place. These molecular rearrangements are associated with energy loss in the form of heat. This energy loss is reflected as the subsequent emergence of a peak in the loss factor. It is worth noting that such values are close to the Tt values measured by DSC (13.0 and 14.4°C for (EI)x2 and (EIS)x2, respectively).

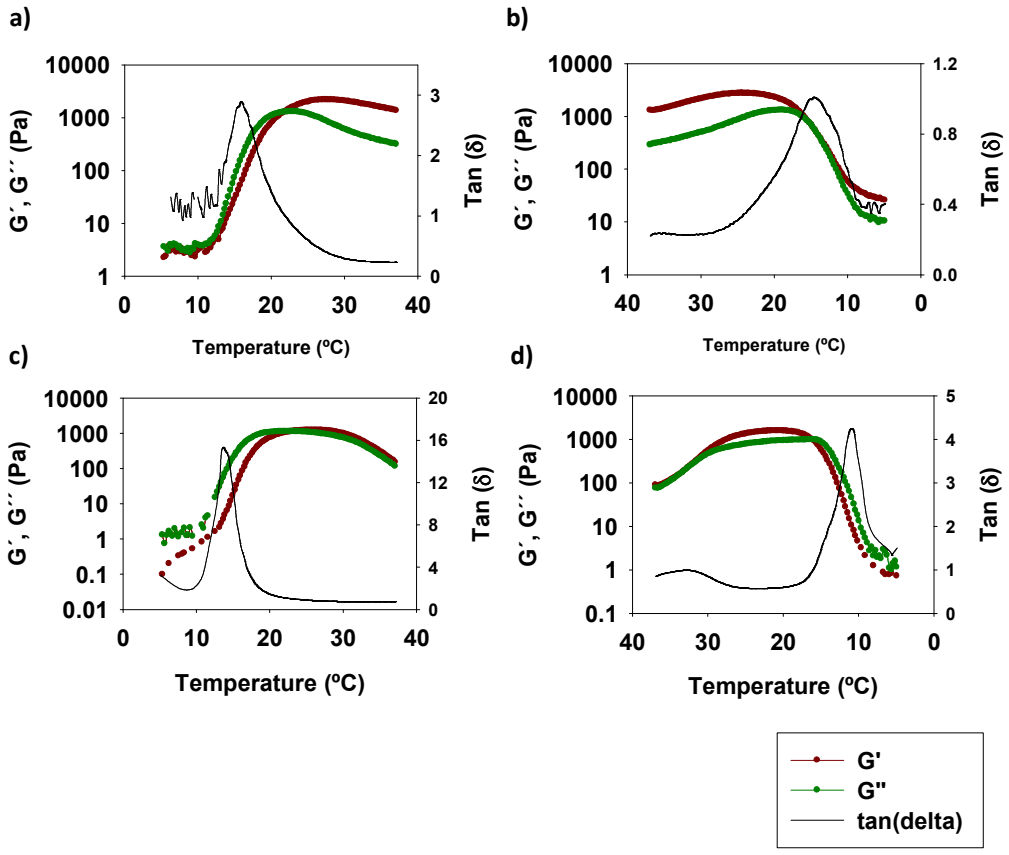

Figure 3: Storage moduli, loss moduli and tanδ (G′, G′′ and tan(δ)) for (EI)x2 and (EIS)x2 co-recombinamer solutions (15 wt.%) as a function of temperature: (a) (EI)x2 during heating; (b) (EI)x2 during cooling; (c) (EIS)x2 during heating; (d) (EIS)x2 during cooling. The samples were heated/cooled at 2.5°C/min in the temperature range from 5 to 37°C. Reversible gel formation occurred for both recombinamers in the temperature range from 10ºC to 20ºC.

The effect of concentration on the reversible thermally triggered gelation process was evaluated by measuring the mechanical properties. To this end, in addition to the already measured 15 wt.% co-recombinamer solutions, 5 wt.% and 10 wt.% (EI)x2 and (EIS)x2 solutions were subjected to heating/cooling cycles (Table 1). In the case of (EIS)x2, for the 10 wt.% concentration and in the temperature range from 10 to 20°C, the formation of a hydrogel took place with a storage modulus of 150 Pa, which is substantially lower than that obtained for the concentration of 15 wt.%. No gelation was observed for the 5 wt.% solution. No gelation was observed for 5 wt.% and 10 wt.% (EI)x2 solutions, which contrasts with the behavior of the (EIS)x2 co-recombinamer, which was able to gel at 10 wt.%. These differences between (EI)x2 and (EIS)x2 again point to an influence of the presence of the SL block in the early gelation process triggered by the EL blocks (VGIPG).

Table 1: Properties displayed by the (EI)x2 and (EIS)x2 reversible hydrogels according to the co-recombinamer concentration. Blank cells indicate no gel formation.

Co-recombinamer	Concentration (%)	Tgel	G'_{max}	G''_{max}
(EI)x2	5	-	-	-
	10	-	-	-

	15	13.9	1100	430
(EIS)x2	5	-	-	-
	10	15.3	150	70
	15	15.8	2500	550

It was therefore concluded that the ITT of the elastomeric part of (EI)x2 and (EIS)x2 leads to the rapid and early formation of a hydrogel, although the presence of SL blocks exerts an indirect influence on such reversible temperature-triggered gelation.

Once the reversible nature of the thermogelling process experienced by both recombinamers had been confirmed, the gelation time was estimated by rheological methods by application of an isotherm at 37 ºC to a sample initially kept at 5 ºC. As shown in Figure 4, the gelation time at 37°C was less than 30s for both co-recombinamer solutions. Since the solutions were able to form a gel within such a short period, both materials are potential candidates for use as injectable hydrogels. Moreover, such a short gelation time would presumably avoid leaking events once the biomaterial is injected, with the consequent advantages for its application, such as a reduction in losses and misallocation of active components, with a concomitant improvement in treatment efficacy.

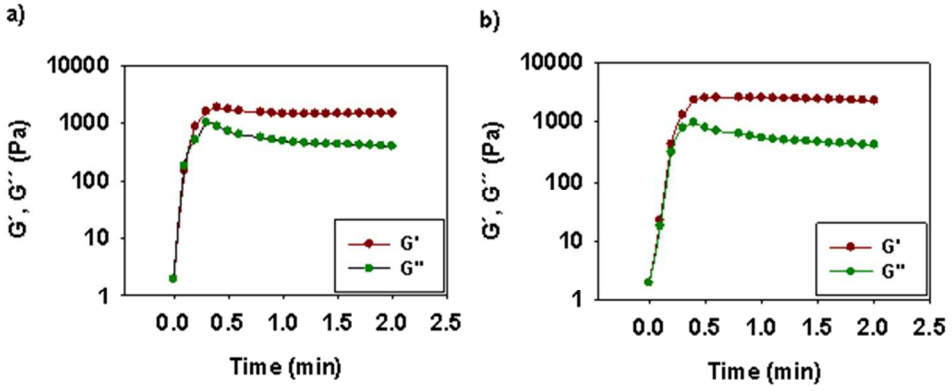

Figure 4: Isotherms for both co-recombinamer solutions at 37 ºC. (a) (EI)x2 at 15 wt.% and (b) (EIS)x2 at 15 wt.%. Note the sharp increase in G´ and G´´ values, indicating that the gelation time was less than 30 s for both recombinamer solutions.

Late gelling mediated by the presence of the SL block: Influence of annealing time on the mechanical properties of the hydrogels

Although the mechanical properties of (EI)x2 do not change with annealing time (results not shown), (EIS)x2 hydrogels display a clear increase in mechanical properties with annealing time. Rheological studies on (EIS)x2 hydrogels with annealing times of 1, 2, 5 and 10 days at 37°C were performed and the results compared with those for the hydrogels without any annealing treatment. As can be seen from Figure 5, an increase in annealing time at 37ºC was accompanied by an increase in the mechanical properties (G´ and G´´) at both measurement temperatures (5 and 37°C). Such increase in the mechanical properties agrees with the previously visualized gelation process (Figure 1). Moreover, irrespective of the presence of SL blocks, the EL part remained able to respond to the temperature variation, as reflected in the decrease in the moduli (G´ and G´´) upon lowering the temperature from 37°C to 5°C (Figure 5). These results were consistent with our initial hypothesis that, at 37°C, both elastomeric and SL blocks are involved in crosslinking of the hydrogels with annealing. Lowering the temperature of the hydrogels to 5°C would exclude the effect of crosslinking by the elastomeric (VGIPG) motifs, thereby explaining the observed reduction in the moduli.

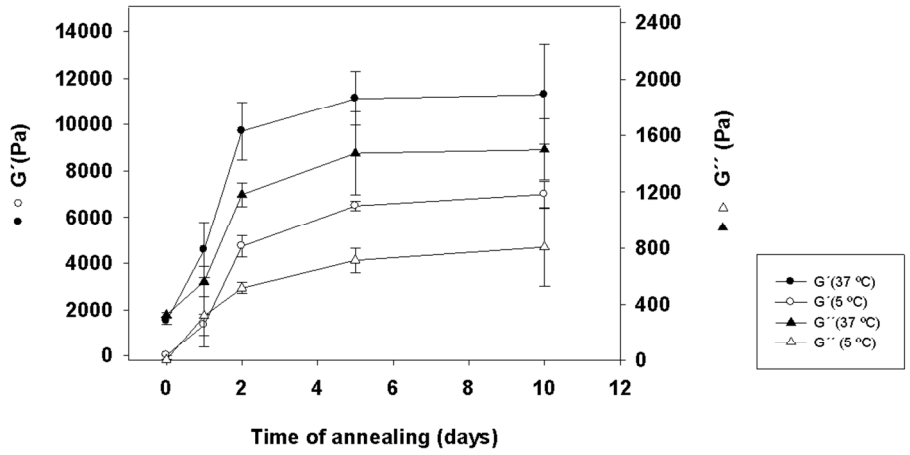

Figure 5: Rheological properties for (EIS)x2 hydrogels measured at 5°C and at 37°C with different annealing times at 37ºC. The data shows an increased in the mechanical properties at both temperatures as the annealing time is increased.

As expected, the mechanical properties displayed by the (EIS)x2 hydrogels are concentration-dependent (Figure 6). This is true for both fresh and annealed samples under all annealing conditions. As an example, the values for an annealing time of 5 days are plotted in Figure 6. The G´ and G´´ values for that annealing time for 5 wt.%, 10 wt.%, and 15 wt.% (EIS)x2 samples showed the expected increase in G´ and G´´ as a function of concentration. It should be noted, however, that the trend shown by the shear modulus is not linear. The increase in G' and G'' (slope of the curves in Figure 6) is higher for higher concentrations, thereby indicating that the increase in modulus is not just the proportional consequence of the increase in mass of the solid phase of the hydrogel.

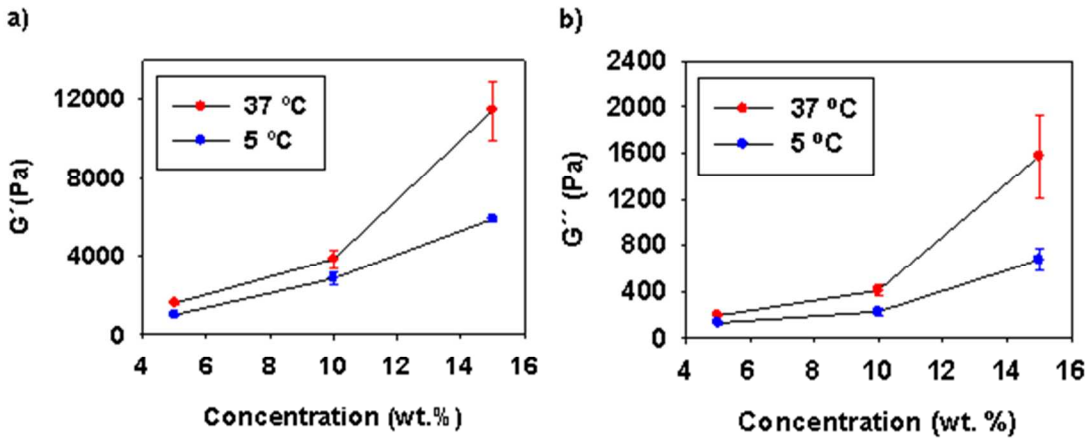

Figure 6: Representation of G´ (a) and G´´ (b) for (EIS)x2 hydrogels annealed at 37ºC at different concentrations. The measurements were carried out at 5 °C and at 37 °C. Note the increase in G´ and G´´ values at both temperatures with increasing the concentration.

In conclusion, the rheology tests performed demonstrate that the (EIS)x2 hydrogel exhibits a dual gelling behavior. Thus, (EIS)x2 undergoes an early gelation due to the reversible ITT of the (VGIPG) block and then experiences an increase in its consistency as a result of annealing. As the only difference between the two materials is the presence of SL blocks in the (EIS)x2, this later maturation must be caused by these blocks. The following group of experiments is aimed at gathering information at a molecular and microscopic level to unveil the molecular and structural events that give rise to the macroscopic properties described above.

Molecular level: FTIR analysis

An FTIR analysis was performed to detect whether the changes experienced by the (EIS)x2 co-recombinamer with annealing time and the previously described macroscopic observations are related to changes in the conformational state of the molecule. IR spectra were obtained (as described in Materials and Methods Section) for samples annealed at 37°C for different times in order to determine whether the maturation process on annealing could also be related to molecular events. The FTIR spectra obtained are shown in Figure 7. The region of the infrared spectrum between 1600 and 1700 cm^{-1} is assigned to the amide I vibration of the peptide backbone [46-48]. This amide I region corresponds to the C=O stretching vibration, which is directly related to the secondary structure of the protein backbone and is commonly used for the quantitative analysis of different secondary structures [49]. Annealed

(EIS)x2 samples underwent a shift of the amide I band towards the 1600-1640 cm^{-1} region with respect to the control (unannealed (EIS)x2). Thus, while the peak for both (EI)x2 and (EIS)x2 without annealing is found at 1626 cm^{-1}, that for (EIS)x2 shifts towards lower wavenumbers (1624 cm^{-1}) after annealing for three days. This shift is more pronounced for the sample annealed for five days (1620 cm^{-1}). This difference is significant ($p < 0.01$). According to the literature, the region between 1600 and 1640 cm^{-1} is related to the presence of β sheets [48]. The signals that appear in the region 1640-1660 cm^{-1} are associated with the presence of random coils and α-helices. The remaining parts of the spectra (1660-1690) are dominated by vibrations due to β-turn structures [48]. Consequently, the observed shift in frequency between the control and annealed samples is indicative of the formation of β-sheet structures [48].

On the other hand, methanol treatment has been reported to promote the formation of β-sheets [50,51]. However, no significant differences were detected between the sample annealed for 5 days and that annealed for 5 days plus methanol treatment. Therefore, methanol treatment did not further increase the displacement of the amide I band toward the region 1640-1600 cm^{-1}, thereby indicating that β-sheet formation reaches a maximum extension simply by annealing. This fact was also supported by the DSC experiments and rheological measurements, with no further changes being detected after annealing for five days at 37ºC, thus showing that the maturation phase had reached stability.

In light of these results, it is evident that the macroscopic differences found between (EI)x2 and (EIS)x2 are likely caused by the SL block and, more precisely, by its tendency to form β-sheets. As they are based on hydrogen bonding, β-sheets provide stronger, more stable, and less dynamic physical cross-links than those found in a flexible network built exclusively on hydrophobic contacts. The double peak found in the DSC endothermic peak upon heating must therefore be understood as the result of an increase in the hydrophobic environment of the EL blocks directly linked to SL blocks already incorporated into β-sheets. β-sheet formation causes a change in the peptides involved, shifting from a

water-soluble to a water-insoluble state. This reflects a decrease in the effective hydrophilicity of the SL blocks after incorporation into the β-sheet structure and, therefore, as they are coupled to the EL blocks, a decrease in the mean hydrophilicity of the (EIS)x2 molecule as a whole. Additionally, formation of the β-sheet structures could also somehow disconnect the hydrophobic EL blocks from the hydrophilic ones. In any case, both effects would cause Tt to decrease, as observed.

In light of the previous results, it is important to question whether the presence of such β-sheets has any consequences, in terms of structure growth, at the nanometric and micrometric level. The following set of experiments were designed to explore these effects.

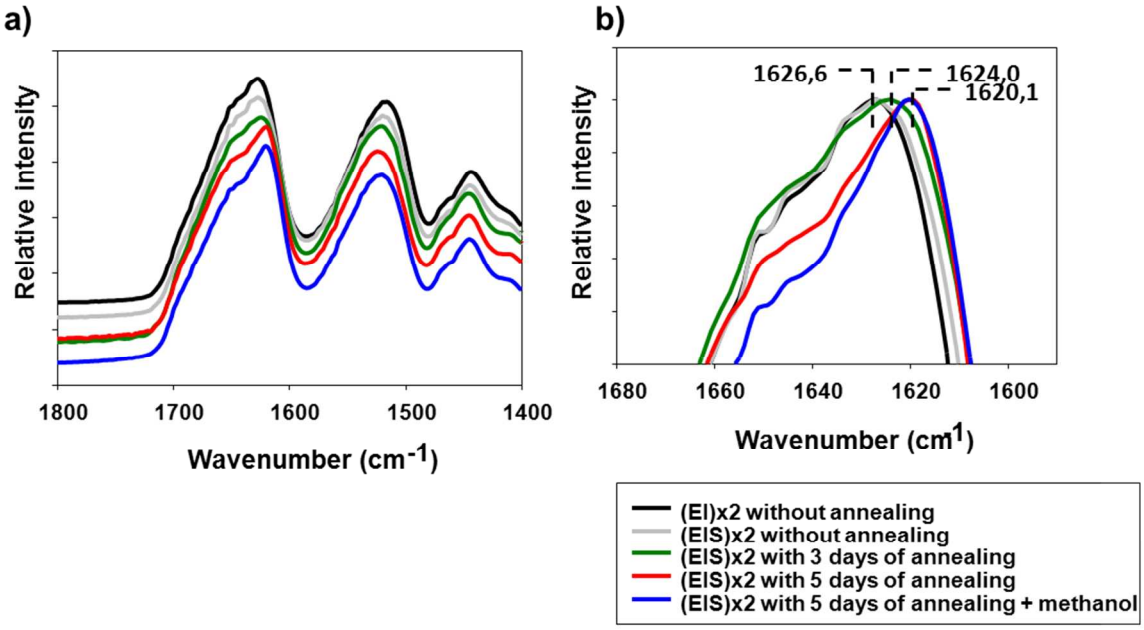

Figure 7: FTIR absorbance spectra of (EIS)x2 samples: a) FTIR spectrum of amide I and amide II region; b) magnified view of the peaks in the amide I region. Grey: Untreated (EI)x2. Black: Untreated (EIS)x2. Green: (EIS)x2 after annealing for three days. Red: (EIS)x2 after annealing for five days. Blue:

(EIS)x2 after annealing for five days and treatment with methanol for two hours. The shift towards lower wavenumbers with increasing annealing time is indicative of the formation of β-sheets.

Dynamic Light Scattering

Dynamic Light Scattering (DLS) was performed in order to check whether characteristic and differential self-assembled nanostructures were formed by the recombinamers studied as a consequence of an increase in temperature above and below Tt and also when annealed at 37ºC at different times. DLS measurements were carried out using dilute samples so as to provide information on the basic structural elements that might form as a consequence of potential self-assembly processes triggered by the formation of hydrophobic contacts and β-sheets.

Figure 8 shows the intensity measurements obtained for samples at 5 and 37ºC (below and above Tt) for both recombinamers after annealing at 37ºC for different times. As regards (EI)x2 without annealing, no nanostructure is detected at 5°C, whereas an increase in intensity is observed upon increasing the temperature to 37ºC, thus indicating the presence of scattering particles. However, as the annealing time increases, the intensity of (EI)x2 remains unchanged for at least 7 months, thereby providing evidence for the high stability of these particles and their independency on annealing. In contrast, (EIS)x2 exhibits an increase in intensity at both temperatures (5 and 37ºC) with increasing annealing time at 37ºC. This increase is not progressive and is more pronounced at shorter annealing times (first week), finally stabilizing from 28 days onwards (Figure 8), remaining stable for at least 7 months. Interestingly, the evolution of intensity with annealing time (Figure 8) seems to follows the same trend as that shown by the progression of the rheological properties (Figure 5), although the stabilization time is considerably higher for the DLS experiments. This is most likely due to the different concentrations used for both techniques (much lower for the DLS experiments).

A temperature change from 5 to 37ºC has a clear effect on intensity for the studied annealing time in all cases (Figure 8).The intensity increase observed upon increasing the temperature from below to above Tt for in (EIS)x2 has a similar value (22.82 ± 2.12 a.u.) to that displayed by (EI)x2 (18.86 ± 0.35 a.u.), thereby indicating that the transition of the elastomeric part remains operational during the whole annealing period studied at this concentration (25 μM).

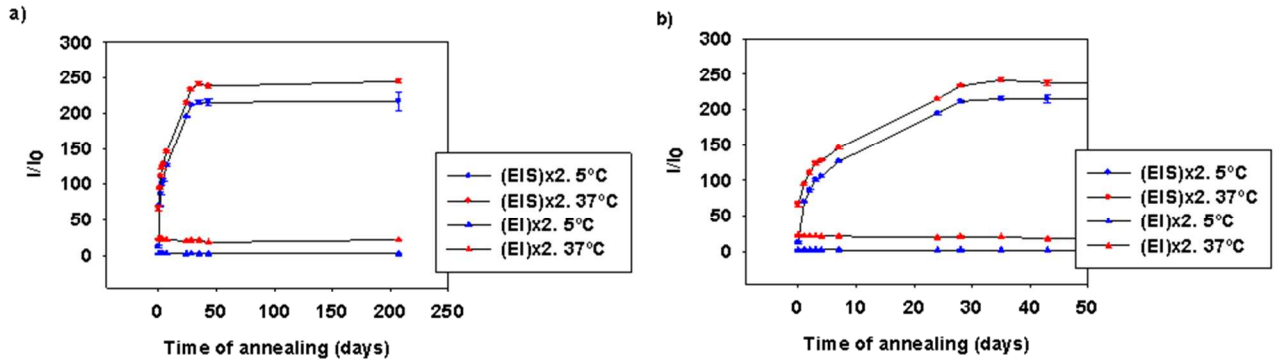

Figure 8: Variation in relative scattered light intensity with annealing time for (EI)x2 (triangles) and (EIS)x2 (circles). B) Magnified view of the first 45 days of annealing. Measurements were carried out at 5ºC (blue) and 37ºC (red). The graph indicates an increase in intensity with increasing annealing time until stabilization is achieved from 28 days onwards.

The particle-size and volume distributions for both recombinamers at two different temperatures (5ºC and 37ºC) are shown in Figure 9. (EI)x2 nanoparticles with a diameter of 35 nm are formed upon increasing the temperature from 5 to 37ºC for both a fresh solution (without annealing) and the sample annealed for a long time (7 months). Intermediate annealing times also showed the same particle size (result not shown), thereby indicating the long-term stability of these particles as well as their lack of evolution. The polydispersity values of 0.05 obtained indicate a low variation in particle size under those conditions for (EI)x2. Nanoparticles of a similar size to those formed by (EI)x2 were detected for (EIS)x2 under non-annealing conditions and at 37ºC. However, the major difference arising as a result of annealing at 37ºC can be seen from the size distribution, which adopts a clearly different and more

complex profile, thereby pointing to the existence of a more heterogeneous population, with higher polydispersity values of 0.3.

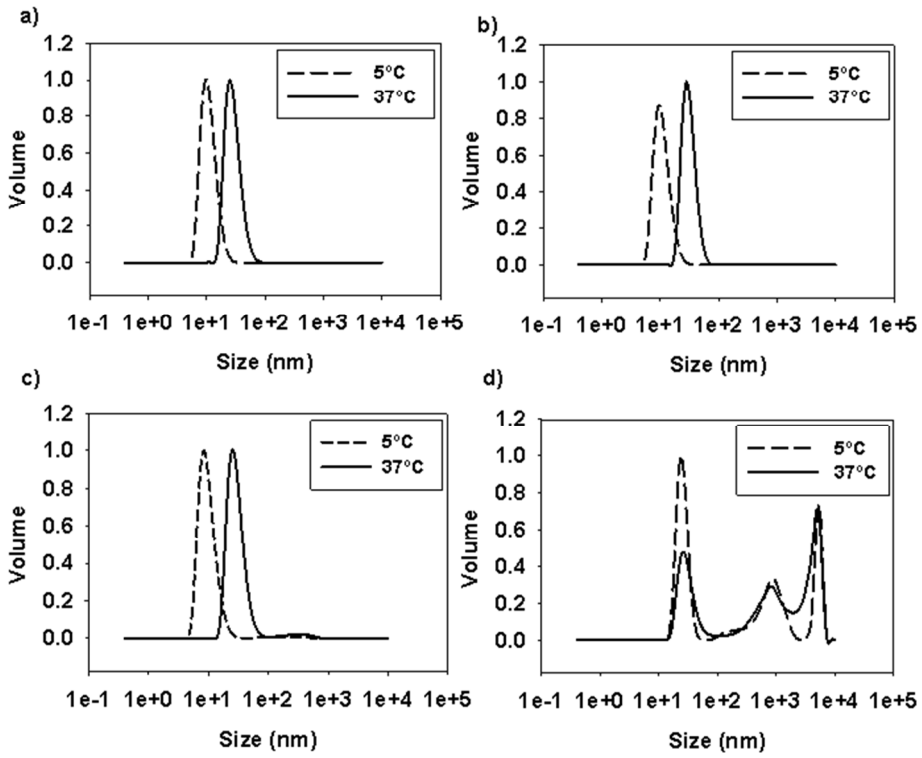

Figure 9: Volume distributions measured at 5 and 37ºC for (EI)x2 and (EIS)x2 without annealing and after annealing for 7 months at 37ºC: a) (EI)x2 without annealing; B) (EI)x2 after annealing for 7 months; c) (EIS)x2 without annealing; d) (EIS)x2 after annealing for 7 months. Results show that (EI)x2 volume profile remains unchanged after annealing, whereas (EIS)x2 adopts a more complex profile, suggesting the presence of a more heterogeneous population.

In light of the above, the differential evolution found initially at the macroscopic level, and subsequently at the molecular level for both co-recombinamers has a parallel at the nanometric level. As deduced from the DLS measurements, annealing causes substantial changes in the geometrical characteristics of

the emerging structures resulting from the two self-assembly processes existing in these samples, i.e., hydrophobic associations in both co-recombinamers and β-sheet formation in (EIS)x2.

Microscopic observation

Transmission electron (TEM) and atomic force microscopy (AFM) were used to visualize the structures suggested by the previous LS studies. The TEM images for (EI)x2 indicate the ability of this co-recombinamer to form spherical nanoparticles. The ability of this kind of amphiphilic ELRs to form micelles and spherical vesicles has previously been reported for closely related di- and triblock co-recombinamers [52-54] and other ELRs [55,56]. The topographical features of these (EI)x2 nanoparticles remain unchanged despite increased incubation at 37ºC (Figure 10, a) to d)). These findings are in agreement with the DLS measurements, which showed that the scattering patterns were stable for at least 7 months.

The TEM images of (EIS)x2 reveal the emergence along annealing of an additional and different structure. Thus, (EIS)x2 is able to self-assemble into nanofibers. The formation of such fibrillar structures is not, however, immediate. In agreement with the DLS data, the only structures found for the freshly prepared solution (no annealing) are micelles. However, fibers start to appear over time (Figure 10, e) to h)) and their population increases with annealing time at the expense of the micelle population. At intermediate annealing times, the co-existence of both populations is evident (see for example Figure 10f). The mutual presence of micelles and fibers would be in agreement with the behavior found in DSC (Figure 1a and b). Finally, after 96 h at 37ºC, a dense network of nanofibers is present; micelles can no longer be visualized and the formed fibers are still present for up to at least 7 months (Figure 10h). Fiber diameter distribution is shown in Figure S 8 (Supplementary information).

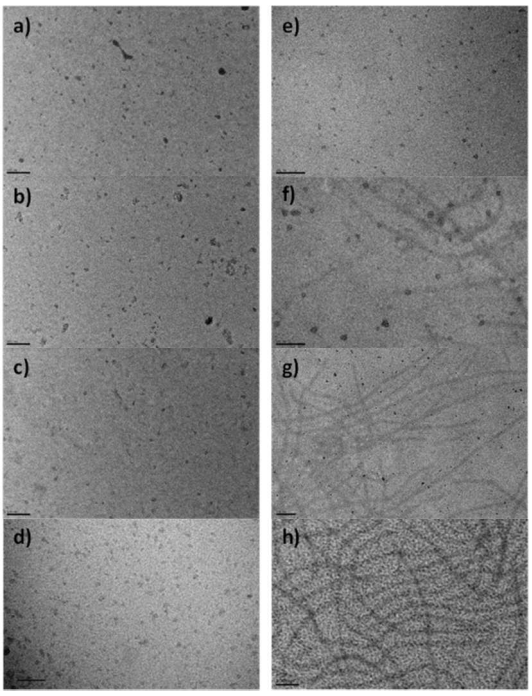

Figure 10: TEM images of the self-assembled nanoparticles formed by (EI)x2 (left) and (EIS)x2 (right) after different annealing times: A) and E) 0 h at 37ºC; B) and F) 48 h at 37ºC; C) and G) 96 h at 37ºC; D) and H) Seven months at 37ºC. Images show that (EIS)x2 evolves from a micellar to a fiber-like state. On the contrary, (EI)x2 invariably displays a spherical shape. Scale bar: 100 nm.

AFM was used to further observe and confirm such different morphologies. As shown in Figure 11, (EI)x2 forms spherical nanoparticles at 37ºC under both conditions (without annealing and after annealing at 37ºC for 7 months). In contrast, (EIS)x2 initially self-assembles into spherical nanoparticles but, after long annealing times, subsequently adopts a fibril shape. These data corroborate the results obtained by DLS and TEM analysis. Interestingly, some of these images may provide clues as to the mechanism of transformation of the micellar structures into fibers. In Figure 11 c, which was obtained for a freshly prepared (EIS)x2 solution (no annealing), the main structural feature is micelles but the alignment of some of these micelles seems to be occurring prior to the fusion and reorganization of the

aligned micelles into fibers. The detailed molecular events taking place during this structural transition are intriguing and deserve further study.

Therefore, as can be concluded from the microscopic observations, (EIS)x2 ultimately self-assembles into a nanofibrillar morphology in an annealing time-dependent manner. These results are in agreement with the DLS measurements. Taking the DLS and TEM/AFM results together, there is clear evidence that the increase in the presence of these fibril structures with increasing annealing time results in the observed increase in scattering intensity, size distribution profiles, and polydispersity for (EIS)x2 in the bulk state.

Other SELRs have been reported to form nano-objects with different shapes, ranging from nanoparticles to nanofibers, depending on the conditions and the SL to EL ratio [28,57,58]. Along with the reported evidence for other SELRs and their ability to spontaneously form fibers, and considering that the only difference between (EI)x2 and (EIS)x2 is the presence of SL blocks in the latter, it can be concluded that these blocks are responsible for the ability of these materials to eventually organize into fibrils under the conditions studied. Such nanofibrillar structure resembles those present in the natural ECM. Therefore, (EIS)x2 has proven to be able to display a complex and orchestrated self-organization process initially based on a rapid gelation, which is structurally based on bridged micelles and finally evolves into a fibrillar structure. It is noteworthy that such fibrillar structures emerge from a previous micelle-based hydrogel rather than from a solid precipitate, as is common in other fiber-forming polypeptides [59].

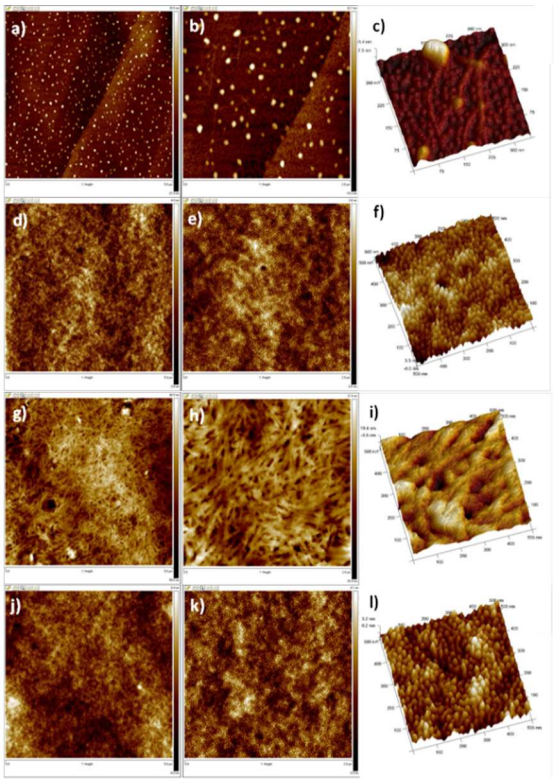

Figure 11: Representative AFM images of the nanostructures derived from (EIS)x2 and (EI)x2 deposited on an HOPG surface: a) to c) (EIS)x2 without annealing. Micellar nanostructures are the predominant population although incipient fibers are discerned. Scanning windows are 5x5 μm, 2x2 μm and 0.5x0.5 μm respectively; d) to f) (EI)x2 without annealing. Images indicate the presence of micellar-like nanoparticles. Scanning windows are 5x5 μm, 2x2 μm and 0.5x0.5 μm respectively; g) to i) (EIS)x2 after annealing for 7 months. Images show the formation of a nano-fibrillar network. Scanning windows are 5x5 μm, 2x2 μm and 0.5x0.5 μm respectively; j) to l) (EI)x2 after annealing for 7 months. Note that micellar like nanoparticles are still present. Scanning windows are 5x5 μm, 2x2 μm and 0.5x0.5 μm respectively.

Coupling of the two gelling processes

Finally, our aim was to determine whether there was any interdependence between the two gelling mechanisms displayed by (EIS)x2. Thus, to elucidate whether the folding and fiber-arrangement kinetics of the SL motifs present in the (EIS)x2 co-recombinamer was dependent exclusively on the temperature or if, by contrast, the conformational state of EL blocks also influenced the folding of the SL blocks, a final set of experiments were carried out. The transformation between the micellar gel and the fibrous gel is followed by a change in the ratio between the secondary peak (I_2) and the main peak (I_1) in the DSC thermograms, assuming that the secondary peak is related to the content of the fibrous phase whereas the primary peak corresponds to the micellar phase. Kinetic analyses were carried out for the (EIS)x2 sample at different annealing temperatures (5, 10, 15, 25, and 60°C) above and below Tt. The I_2/I_1 ratio for the different thermograms obtained at different annealing times for each fixed temperature can be seen in Figure 12, a. Using these values in a kinetics analysis showed a suitable fit for the k values obtained with the Arrhenius equation at annealing temperatures above Tt (Figure 12,b). However, when the whole range of temperatures is analyzed, lower temperatures (5 and 10°C) are completely out of trend, displaying much lower values, with a clear step around Tt (Figure 12, b). According to these data, the kinetics of the transformation from micellar to fibrous gel is influenced by both temperature and the conformational state of the co-recombinamer; more specifically, the folded or unfolded state of the EL blocks plays a critical role. Therefore, although the formation of β-sheets and the fibrillar structure can, in principle, take place without any contribution from the EL blocks, in practice this transformation takes place very slowly. However, prior folding of the EL blocks promotes an increase in the rate of fibril formation, clearly indicating how these two, in principle, independent molecular events are concomitant and strongly connected. We can hypothesize that such concomitant interplay between these two molecular events is facilitated by the spatial approximation of the SL blocks caused by the micellation driven by the EL blocks. It is also plausible that the recombinant nature

of (EIS)x2, which means that all the molecules are identical in all aspects, including the regular arrangement of the SL and EL blocks, facilitates this coupling of the two processes. Therefore, interestingly, the folding of the EL block is effectively controlling the subsequent self-organization of the SL blocks, thus meaning that these two processes are, in practice, consecutive and interdependent.

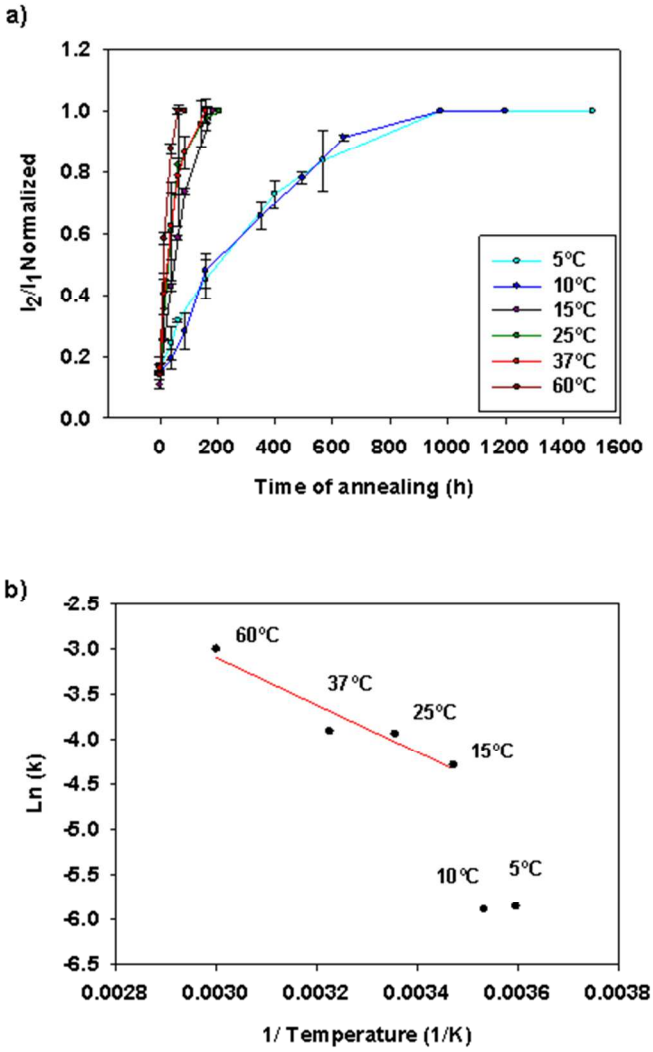

Figure 12: Evaluation of the folding kinetics of SL blocks. a) Representation of the ratio between the secondary peak (I_2) and the main peak (I_1) in the thermograms obtained for (EIS)x2 samples after different annealing times at the specified temperatures. b) Representation of the two variables of the

Arrhenius equation in order to check the linearity of their dependence. Data show a suitable fit for the "k" values obtained with the Arrhenius equation at annealing temperatures above Tt.

CONCLUSIONS

(EIS)x2 is constituted by a combination of EL blocks and SL blocks, with the first ones being already arranged in a tetrablock, thermally triggered, amphiphilic molecule. Another distinctive feature of this composition is that the EL blocks are predominant. As a result of its peculiar composition, this material is able to self-organize from a sol state to a fibrous gel state. This atypical sol-gel transition is characterized by a complex and orchestrated sequence of molecular events displayed by this molecule. This multistage process is initially triggered by an increase in temperature, which induces the self-assembly of the EL blocks as a result of their characteristic ITT. This first step is distinguished by its instantaneity and is dominated by reversible hydrophobic aggregation of the (VGIPG) block. This first stage leads to a soft gel ($G'=2.5\cdot10^3$ Pa) in which a reversible, bridged micellar structure is the main feature. The second stage of this sequence starts at this point: folding of the EL block strongly favors the interaction between the SL blocks and the emergence of irreversible beta-sheet structures. These markedly alter the mode and stability of the hydrogel, which becomes harder ($G'= 1\cdot10^4$ Pa). The kinetics of this maturation is slower than that of the first stage. Finally, as a consequence of the maturation of the β-sheet arrangements, the hydrogel gives rise to the emergence of a fibrillar structure. Furthermore, the nanofibrillar architecture adopted by the complex self-organization process of this co-recombinamer emulates the structural organization of the native ECM. In addition, their proven stability, even in environments with a high fluid content, together with their convenient multistage gelation kinetics, makes these hydrogels excellent candidates for use as injectable hydrogels for biomedical applications. This potential is further supported by the excellent properties of ELRs in

general. Finally, due to the recombinant nature of this SELR, it is easy to build an extensive –battery of different bioactive versions that can incorporate, at the gene level, relevant peptide-based biological cues such as specific cell-adhesion sequences and metalloprotease recognition sites, amongst others. These materials therefore constitute a new versatile family of hydrogels that can be used for many different applications and therapies, both *in vitro* and *in vivo*, and may also serve as model artificial cellular niches for cell studies and production.

SUPPORTING INFORMATION AVAILABLE

SDS-PAGE analysis, MALDI-TOF spectra, amino acid composition for the (EIS)x2, evaluation of the transparency and porous structure by SEM are supplied as Supporting Information. "This material is available free of charge via the Internet at http://pubs.acs.org."

AUTHOR INFORMATION

Corresponding Author

* E-mail: roca@bioforge.uva.es

Author Contributions

The manuscript was written through contributions of all authors. All authors have given approval to the final version of the manuscript.

ACKNOWLEDGMENT

We acknowledge financial support from the EU through the European regional development fund (ERDF), from the MINECO (MAT2013-41723-R y MAT2013-42473-R, PRI-PIBAR- 2011-1403, and MAT2012-38043), the JCyL (projects VA049A11, VA152A12, and VA155A12), the CIBER-BBN, the JCyL, and the Instituto de Salud Carlos III under the Network Center of Regenerative Medicine and Cellular Therapy of Castilla and Leon.

This work is dedicated to the memory of Prof. Isabel M. Lopez.

REFERENCES

(1) Zhao, Y.; Sakai, F.; Su, L.; Liu, Y.; Wei, K.; Chen, G.; Jiang, M. *Adv. Mater.* **2013**, *25*, 5215-5256.

(2) Lutolf, M. P.; Hubbell, J. A. *Nat. Biotechnol.* **2005**, *23*, 47-55.

(3) Hubbell, J. A. *Curr. Opin. Biotechnol.* **2003**, *14*, 551-558.

(4) Stevens, M. M.; George, J. H. *Science* **2005**, *310*, 1135-1138.

(5) Discher, D. E.; Janmey, P.; Wang, Y. L. *Science* **2005**, *310*, 1139-1143.

(6) Swift, J.; Ivanovska, I. L.; Buxboim, A.; Harada, T.; Dingal, P. C.; Pinter, J.; Pajerowski, J. D.; Spinler, K. R.; Shin, J. W.; Tewari, M.; Rehfeldt, F.; Speicher, D. W.; Discher, D. E. *Science* **2013**, *341*, 1240104.

(7) Khetan, S.; Guvendiren, M.; Legant, W. R.; Cohen, D. M.; Chen, C. S.; Burdick, J. A. *Nat. Mater.* **2013**, *12*, 458-465.

(8) Rodríguez-Cabello, J. C.; Martín, L.; Alonso, M.; Arias, F. J.; Testera, A. M. *Polymer* **2009**, *50*, 5159-5169.

(9) Urry, D. W. *Angew. Chem., Int. Ed. Engl.* **1993**, *32*, 819-841.

(10) Tamburro, A. M.; Guantieri, V.; Pandolfo, L.; Scopa, A. *Biopolymers* **1990**, *29*, 855-870.

(11) Urry, D. W.; Parker, T. M.; Reid, M. C.; Gowda, D. C. *J. Bioact. Compat. Polym.* **1991**, *6*, 263-282.

(12) Rodriguez-Cabello, J. C.; Martin, L.; Girotti, A.; Garcia-Arevalo, C.; Arias, F. J.; Alonso, M. *Nanomedicine* **2011**, *6*, 111-122.

(13) Rodriguez-Cabello, J. C.; Pierna, M.; Fernandez-Colino, A.; Garcia-Arevalo, C.; Arias, F. J. *Adv. Biochem. Eng./Biotechnol.* **2010**, *125*, 145-179.

(14) Martin, L.; Arias, F. J.; Alonso, M.; Garcia-Arevalo, C.; Rodriguez-Cabello, J. C. *Soft Matter* **2010**, *6*, 1121-1124.

(15) Betre, H.; Liu, W.; Zalutsky, M. R.; Chilkoti, A.; Kraus, V. B.; Setton, L. A. *J. Controlled Release* **2006**, *115*, 175-182.

(16) Liu, W.; MacKay, J. A.; Dreher, M. R.; Chen, M.; McDaniel, J. R.; Simnick, A. J.; Callahan, D. J.; Zalutsky, M. R.; Chilkoti, A. *J. Control Release* **2010**, *144*, 2-9.

(17) Betre, H.; Setton, L. A.; Meyer, D. E.; Chilkoti, A. *Biomacromolecules* **2002**, *3*, 910-916.

(18) Betre, H.; Ong, S. R.; Guilak, F.; Chilkoti, A.; Fermor, B.; Setton, L. A. *Biomaterials* **2006**, *27*, 91-99.

(19) Quynh P. Pham, U. S., Dr. Antonios G. Mikos *Tissue Eng.* **2006**, *12*, 1197-1211.

(20) Zhang, S. *Nat. Biotech.* **2003**, *21*, 1171-1178.

(21) Altunbas, A.; Pochan, D. J. In *Peptide-Based Materials.*; Deming, T., Ed.; Springer Berlin Heidelberg: Los Angeles, 2011; p 174.

(22) Takahashi, Y.; Gehoh, M.; Yuzuriha, K. *Int. J. Biol. Macromol.* **1999**, *24*, 127-138.

(23) Asakura, T.; Yao, J.; Yamane, T.; Umemura, K.; Ulrich, A. S. *J. Am. Chem. Soc.* **2002**, *124*, 8794-8795.

(24) Hardy, J. G.; Römer, L. M.; Scheibel, T. R. *Polymer* **2008**, *49*, 4309-4327.

(25) Altman, G. H.; Diaz, F.; Jakuba, C.; Calabro, T.; Horan, R. L.; Chen, J. S.; Lu, H.; Richmond, J.; Kaplan, D. L. *Biomaterials* **2003**, *24*, 401-416.

(26) Cappello, J.; Crissman, J.; Dorman, M.; Mikolajczak, M.; Textor, G.; Marquet, M.; Ferrari, F. *Biotechnol. Prog.* **1990**, *6*, 198-202.

(27) Dinerman, A. A.; Cappello, J.; Ghandehari, H.; Hoag, S. W. *Biomaterials* **2002**, *23*, 4203-4210.

(28) Xia, X. X.; Xu, Q.; Hu, X.; Qin, G.; Kaplan, D. L. *Biomacromolecules* **2011**, *12*, 3844-3850.

(29) Nagarsekar, A.; Crissman, J.; Crissman, M.; Ferrari, F.; Cappello, J.; Ghandehari, H. *J. Biomed. Mater. Res.* **2002**, *62*, 195-203.

(30) Nagarsekar, A.; Crissman, J.; Crissman, M.; Ferrari, F.; Cappello, J.; Ghandehari, H. *Biomacromolecules* **2003**, *4*, 602-607.

(31) Haider, M.; Leung, V.; Ferrari, F.; Crissman, J.; Powell, J.; Cappello, J.; Ghandehari, H. *Mol. Pharmaceutics* **2005**, *2*, 139-150.

(32) Landau, L. D.; Lifshitz, E. M. In *Theory of Elasticity*; 3rd ed.; Kosevitch, A. M., Pitaevskiĭ, L. P., Eds.; Pergamon Press: 1984; p 195.

(33) Leach, J. B.; Wolinsky, J. B.; Stone, P. J.; Wong, J. Y. *Acta Biomater.* **2005**, *1*, 155-164.

(34) Girotti, A.; Fernandez-Colino, A.; Lopez, I. M.; Rodriguez-Cabello, J. C.; Arias, F. J. *Biotechnol. J.* **2011**, *6*, 1174-1186.

(35) Rodriguez-Cabello, J. C.; Girotti, A.; Ribeiro, A.; Arias, F. J. In *Nanotechnology in Regenerative Medicine*; Navarro, M., Planell, J. A., Eds.; Humana Press: 2012; p 319.

(36) Meyer, D. E.; Chilkoti, A. In *Protein Interactions E Golemis, Ed. Cold Spring Harbor Laboratory Press*; 2nd ed.; Golemis, E., Adams, P. D., Eds.; Cold Spring Harbor Laboratory Press: 2002; p 938.

(37) Megeed, Z.; Cappello, J.; Ghandehari, H. *Adv Drug Deliv Rev* **2002**, *54*, 1075-1091.

(38) Machado, R.; Azevedo-Silva, J.; Correia, C.; Collins, T.; Arias, F. J.; Rodriguez-Cabello, J. C.; Casal, M. *AMB Express* **2013**, *3*, 1-15.

(39) Meyer, D. E.; Chilkoti, A. *Nat. Biotechnol.* **1999**, *17*, 1112-1115.

(40) Meyer, E.; Chilkoti, A. In *Protein-Protein Interactions: A Molecular Cloning Manual*; 2nd ed.; Golemis, E., Adams, P. D., Eds.; Cold Spring Harbor Laboratory Press: 2002; p 938.

(41) Urry, D. W.; Gowda, D. C.; Parker, T. M.; Luan, C. H.; Reid, M. C.; Harris, C. M.; Pattanaik, A.; Harris, R. D. *Biopolymers* **1992**, *32*, 1243-1250.

(42) Nystroem, B.; Walderhaug, H.; Hansen, F. K.; Lindman, B. *Langmuir* **1995**, *11*, 750-757.

(43) Tung, C.-Y. M.; Dynes, P. J. *J. Appl. Polym. Sci.* **1982**, *27*, 569-574.

(44) Winter, H. H.; Chambon, F. *J. Rheol.* **1986**, *30*, 367-382.

(45) Anseth, K. S.; Bowman, C. N.; Brannon-Peppas, L. *Biomaterials* **1996**, *17*, 1647-1657.

(46) Hu, X.; Kaplan, D.; Cebe, P. *Macromolecules* **2008**, *41*, 3939-3948.

(47) Hu, X.; Kaplan, D.; Cebe, P. *Macromolecules* **2006**, *39*, 6161-6170.

(48) Hu, X.; Wang, X.; Rnjak, J.; Weiss, A. S.; Kaplan, D. L. *Biomaterials* **2010**, *31*, 8121-8131.

(49) Kong, J.; Yu, S. *Acta Biochim. Biophys. Sin.* **2007**, *39*, 549-559.

(50) Lu, Q.; Hu, X.; Wang, X.; Kluge, J. A.; Lu, S.; Cebe, P.; Kaplan, D. L. *Acta Biomater.* **2010**, *6*, 1380-1387.

(51) Chen, X.; Cai, H.; Ling, S.; Shao, Z.; Huang, Y. *Appl. Spectrosc.* **2012**, *66*, 696-699.

(52) Martín, L.; Castro, E.; Ribeiro, A.; Alonso, M.; Rodríguez-Cabello, J. C. *Biomacromolecules* **2012**, *13*, 293-298.

(53) Pinedo-Martín, G.; Castro, E.; Martín, L.; Alonso, M.; Rodríguez-Cabello, J. C. *Langmuir* **2014**, *30*, 3432-3440.

(54) Dreher, M. R.; Simnick, A. J.; Fischer, K.; Smith, R. J.; Patel, A.; Schmidt, M.; Chilkoti, A. *J. Am. Chem. Soc.* **2007**, *130*, 687-694.

(55) Machado, R.; Bessa, P. C.; Reis, R. L.; Rodriguez-Cabello, J. C.; Casal, M. In *Nanoparticles in Biology and Medicine*; Soloviev, M., Ed.; Humana Press: 2012; p 555.

(56) Bessa, P. C.; Machado, R.; Nürnberger, S.; Dopler, D.; Banerjee, A.; Cunha, A. M.; Rodríguez-Cabello, J. C.; Redl, H.; van Griensven, M.; Reis, R. L.; Casal, M. *J. Controlled Release* **2010**, *142*, 312-318.

(57) Golinska, M. D.; Pham, T. T. H.; Werten, M. W. T.; de Wolf, F. A.; Cohen Stuart, M. A.; van der Gucht, J. *Biomacromolecules* **2013**, *14*, 48-55.

(58) Hwang, W.; Kim, B. H.; Dandu, R.; Cappello, J.; Ghandehari, H.; Seog, J. *Langmuir* **2009**, *25*, 12682-12686.

(59) Fändrich, M. *Cell. Mol. Life Sci.* **2007**, *64*, 2066-2078.

TOC